2019 M6.7 Yamagata-Oki earthquake in the stress shadow of 2011 Tohoku-Oki earthquake: Was it caused by the reduction in fault strength?

Keisuke Yoshida[1], Naoki Uchida[1], Satoshi Hiarahara[1], Takashi Nakayama[1], Toru Matsuzawa[1], Tomomi Okada[1], Yoshiaki Matsumoto[1], Akira Hasegawa[1]

[1]Research Center for Prediction of Earthquakes and Volcanic Eruptions, Graduate School of Science, Tohoku University, Sendai, Japan

Corresponding author: Keisuke Yoshida, Research Center for Prediction of Earthquakes and Volcanic Eruptions, Tohoku University, 6-6 Aza-Aoba, Aramaki, Aoba-ku, Sendai 980-8578, Japan. (keisuke.yoshida.d7@tohoku.ac.jp)

Abstract

Earthquake occurrence in the stress shadow provides a unique opportunity for extracting the information about the physical processes behind earthquakes because it highlights processes other than the ambient stress change in earthquake generation. In this study, we examined the fault structure and the spatiotemporal distribution of the aftershocks of the 2019 M6.7 Yamagata-Oki earthquake, which occurred in the stress shadow of the 2011 M9.0 Tohoku-Oki earthquake, to better understand the earthquake generation mechanism. Moreover, we investigated the temporal evolution of the surface strain rate distribution in the source region by using GNSS data. The earthquake detection and hypocenter relocation succeeded in delineating three planar structures of earthquakes. The results suggest that individual aftershocks were caused by a slip on the macroscopic planar structures. Aftershock hypocenters rapidly migrated upward from the deeper part of the major plane (fault) similar to the recent earthquake swarm sequences triggered by the 2011 Tohoku-Oki earthquake in the stress shadow in the upper plate. East–west contraction strain rate in the source region of the Yamagata-Oki earthquake with E–W compressional reverse fault mechanism changed to the E–W extension as a result of Tohoku-Oki earthquake, and it continued until the occurrence of the Yamagata-Oki earthquake. The upward hypocenter migrations, together with the earthquake occurrence in the stress shadow and in the E–W extension strain rate field, suggest that the reduction in the fault strength due to the uprising fluids contributed to the occurrence of this earthquake sequence. Localized aseismic deformations, such as aseismic creeps, beneath the fault zone may also have contributed to the earthquake occurrence. The results support the hypothesis that aseismic processes in the deeper part of the fault play crucial roles in the occurrence of shallow intraplate earthquakes.

Keywords: Aseismic process, fluid migration, stress shadow, hypocenter relocation, aftershock, 2016 Yamagata-Oki earthquake

1. Introduction

Several destructive earthquakes have occurred during the last 60 years in the active deformation zone along the eastern margin of the Japan Sea, such as the 1964 M7.5 Niigata earthquake, the 1983 M7.7 Nihonkai-Chubu earthquake, and the 1993 M7.8 Hokkaido Nansei-Oki earthquake (Fig. 1). Nakamura (1983) and Kobayashi (1983) hypothesized that this north–south striking deformation zone acts as a nascent plate boundary and releases the accumulated strain energy between the Eurasian and the North American plates. Subsequent seismological and space geodetic observations confirmed a relative plate motion proceeding along this deformation zone (Wei and Seno, 1998; Heki et al., 1999), although there are disagreements about the location and mode of this nascent boundary (Ohtake, 1995) and the microplate structures of both sides (Wei and Seno, 1998; Heki et al., 1999). Complicated fault structures in this deformation zone suggest that the accumulated strain is released by multiple intraplate faults (Ohtake, 1995).

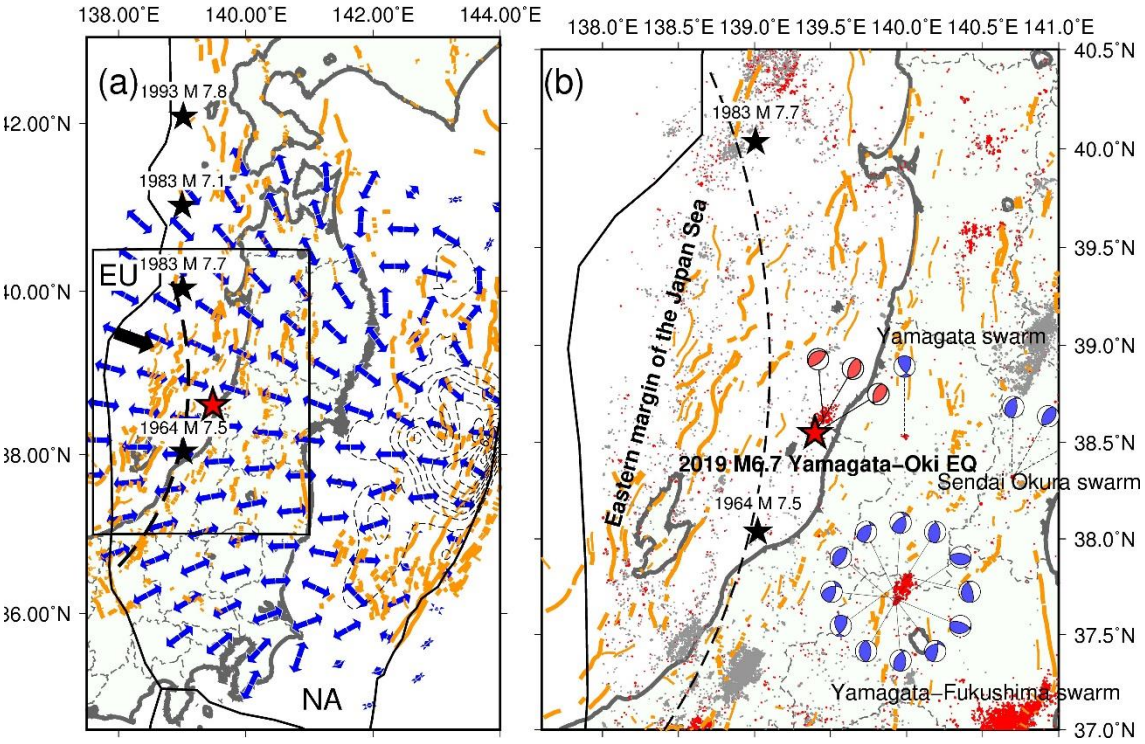

Fig. 1. Maps showing the source region of the 2019 M6.7 Yamagata-Oki earthquake. The red star indicates the hypocenter of the Yamagata-Oki earthquake. Black stars indicate the locations of the 1964 M7.5 Niigata earthquake, 1983 M7.7 Nihonkai-Chubu earthquake and its largest aftershock (M7.1), and 1993 M7.8 Hokkaido

Nansei-Oki earthquake. Numbers above the stars denote the occurrence years and the JMA magnitudes. Orange lines indicate the traces of the active fault. Black thick lines and arrows indicate the plate boundaries and relative plate motions, respectively, according to Bird (2003). In this model, the location of the plate boundary between the Eurasian (or Amur) and North American (or Okhotsk) plates is based on Nakamura (1983). The broken curve indicates the location of this plate boundary proposed by Ohtake (1995). (a) Map showing northeast Japan. Blue arrows show the minimum compressional principle stress axis of the static stress change of the 2011 Tohoku-Oki earthquake (Yoshida et al., 2012). NA: North American plate , EU: Eurasian plate. Broken contour lines show the coseismic slip distribution of the 2011 Tohoku-Oki earthquake (Iinuma et al., 2012). (b) Enlarged view of the rectangle region of (a). Beach balls show the focal mechanisms listed in the F-net catalog (Fukuyama, 1998). Gray and red dots show the hypocenters of shallow earthquakes ($z < 40$ km) with the JMA magnitude $\geq$ 2.0 before and after the 2011 Tohoku-Oki earthquake, respectively, for the period from Jan. 1, 1997 to August 20, 2019.

An M6.7 earthquake occurred west off the border between Yamagata and Niigata prefectures on June 18, 2019 (JST) in this deformation zone, referred to as the 2019 Yamagata-Oki earthquake (Figs. 1–3). The occurrence of this earthquake is enigmatic from the point of view of the temporal evolution of the stress field in this region that was affected by the 2011 M9 Tohoku-Oki earthquake. The state of stress in this deformation zone is the WNW–ESE compressional reverse-faulting regime (Okamura et al., 1995). The 2011 Tohoku-Oki earthquake and the associated postseismic slip reduced this WNW–ESE compressional stress, and the reduced amount of differential stress was estimated to be ~0.5 MPa (Yoshida et al., 2012). Thus, the Tohoku-Oki earthquake created a stress shadow for typical WNW–ESE compressional reverse-fault earthquakes in this deformation zone (Yoshida et al., 2019a). The shear stress magnitude on the fault of the Yamagata-Oki earthquake after the Tohoku-Oki earthquake should be lower than that just before the Tohoku-Oki earthquake. Nevertheless, the M6.7 reverse-fault earthquake occurred in the stress shadow after eight years (3,021 d) from the 2011 earthquake (Fig. 3).

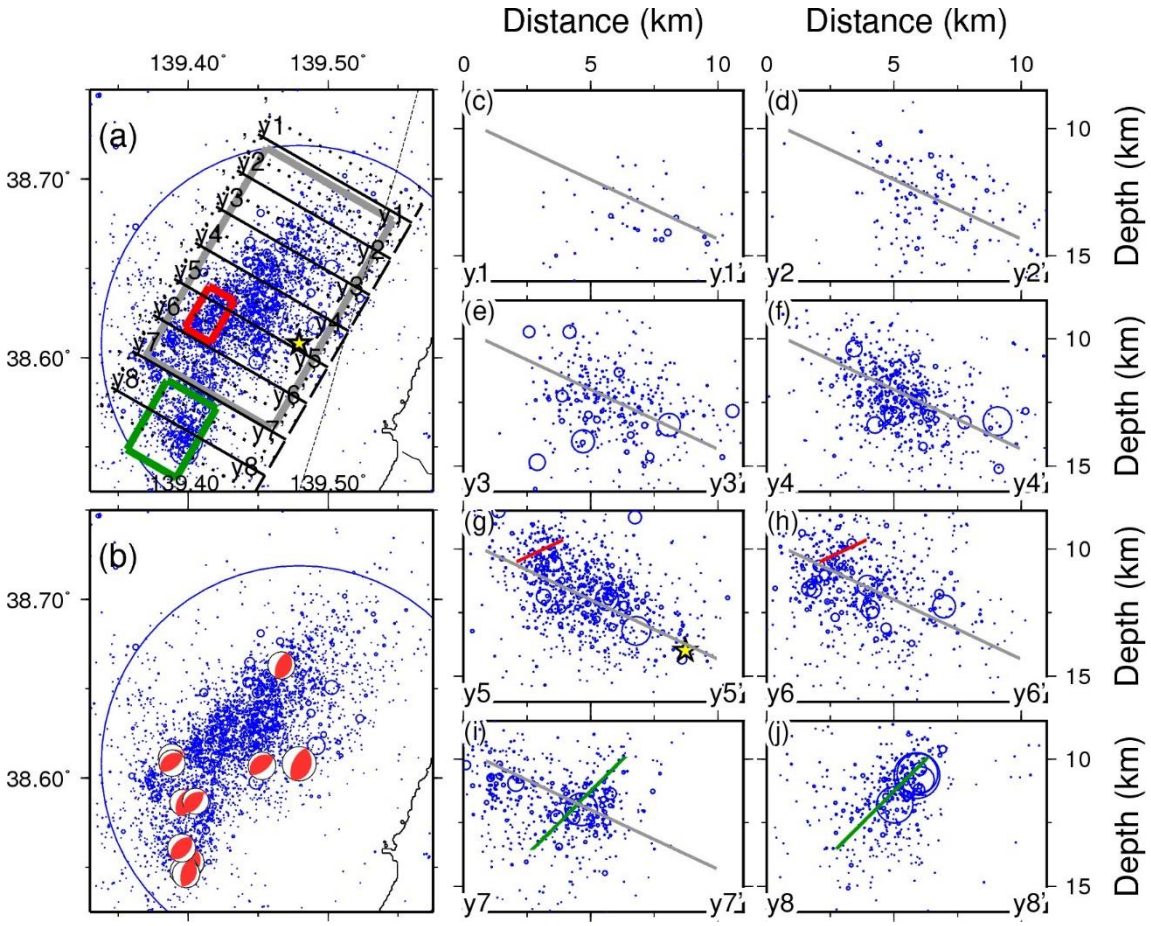

Fig. 2. Distribution of the hypocenters in the Japan Meteorological Agency (JMA) unified catalogue from March 1, 2003 to May 10, 2020. Blue circles represent the hypocenters. The size of each circle corresponds to the diameter of the fault, assuming a stress drop of 3 MPa. The star denotes the hypocenter of the mainshock. (a) A map view showing the focal region of the 2019 Yamagata-Oki earthquake and the hypocenter distribution. (b) A map view showing the focal mechanisms determined by the JMA by red "beach balls." (c)–(j) Cross-sectional views of vertical hypocenter distribution along the lines indicated in (a).

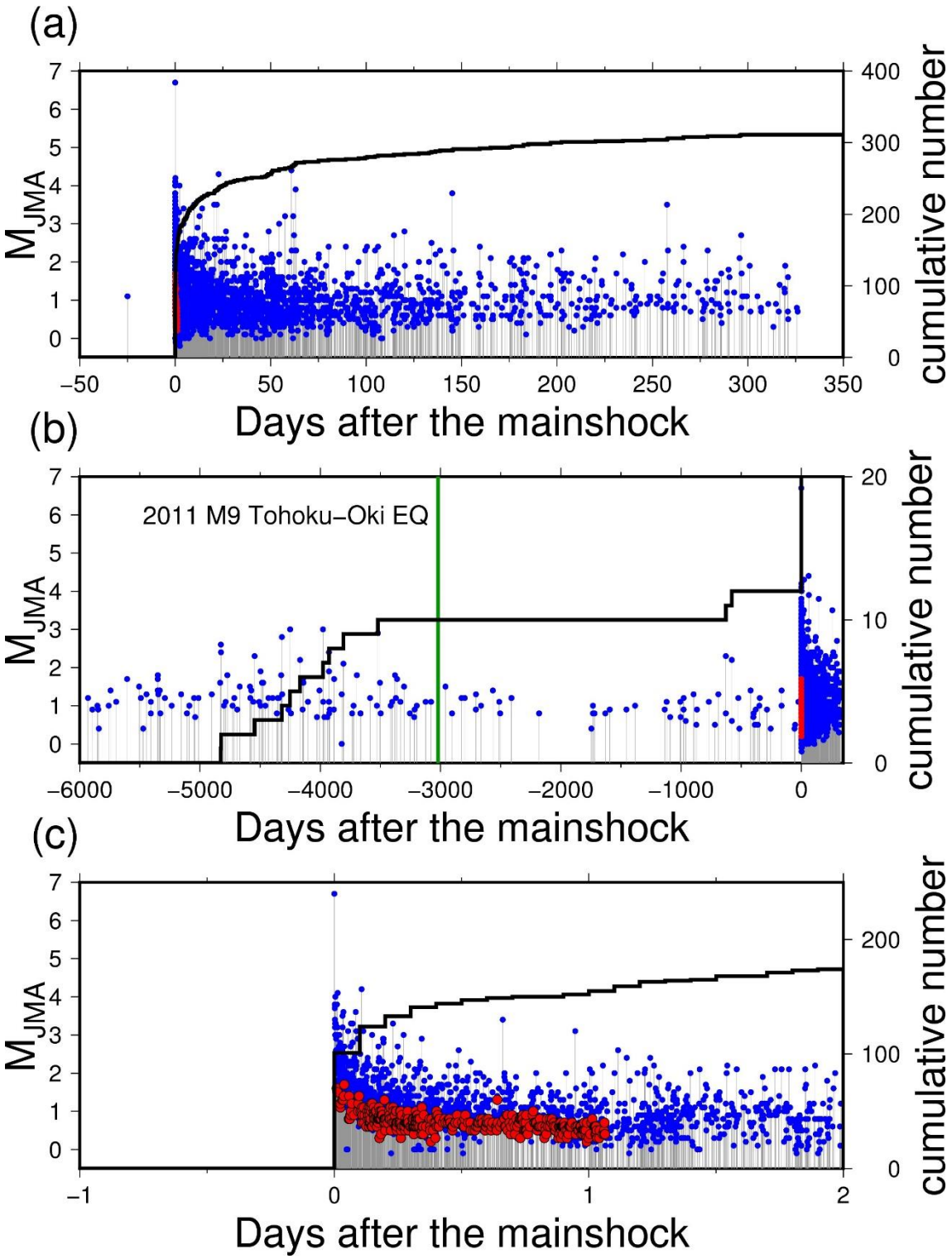

Fig. 3. Magnitude-time diagrams of events in and around the source region of the 2019 Yamagata-Oki earthquake for (a) -50 d to 350 d, (b) -6,000 d to 350 d, and (c) -1 d to 2 d following the mainshock. The blue and red circles with gray bars indicate

the earthquake magnitudes listed in the JMA unified catalogue and those of newly detected in this study, respectively. The black line denotes the cumulative number of earthquakes with magnitudes greater than 2.0. The green vertical line indicates the occurrence time of the 2011 Tohoku-Oki earthquake.

An important argument on the occurrence of shallow intraplate earthquakes is the existence of local sources affecting the states of stress and fault strength of the fault zone (Iio and Kobayashi, 2002). Previous studies suggested the important role of aseismic processes progressing in the deeper part of the fault, including pore pressure migrations and aseismic slips (Rice, 1992; Sibson, 1992; Liu and Zoback, 1997; Iio and Kobayashi, 2002; Hasegawa et al., 2005). Sibson (1992) proposed a model in which the pore pressure cycle associated with the upward fluid migrations controls the earthquake cycle of shallow intraplate earthquakes. In this fault-valve model, a local reduction in the fault strength due to increasing pore pressure is crucial for the occurrence of earthquakes. Iio and Kobayashi (2002) argued that the local stress concentration due to the localized deformation beneath the fault accounts for various geophysical and geological observations. Hasegawa et al. (2005) incorporated these ideas to the deformation model of the arc crust in the subduction zone, in which fluids dehydrated from the subducting slab play central roles.

The occurrence of the M6.7 earthquake in the stress shadow provides a unique opportunity for extracting information about the physical processes behind earthquake generation. This is because the occurrence of earthquakes in the stress shadow highlights the processes other than the ambient stress change in earthquake generation. Previous studies have analyzed several earthquake swarm sequences triggered in the stress shadow of the 2011 Tohoku-Oki earthquake (Fig. 1) and showed the upward migration behavior of hypocenters (Okada et al., 2015; Yoshida and Hasegawa, 2018a and b) along several planar structures; they hypothesized that swarm activities were triggered by the reduction in the fault strength due to the upward migration of the pore pressure despite the reduction in the shear stress. This hypothesis is consistent with the model proposed for northeast Japan, in which the slab-derived fluids that have reached the crust play a central role (Hasegawa et al., 2005).

In this study, we investigated the aftershock activities of the 2019 M6.7 Yamagata-Oki earthquake that occurred in the stress shadow of the 2011 M9.0 Tohoku-Oki earthquake to understand the earthquake generation mechanism. We detected early aftershocks that relocated the hypocenters and determined the focal mechanisms of

151 earthquakes in the source region (Section 2). Moreover, we examined the temporal
152 evolution of strain rates after the 2011 Tohoku-Oki earthquake. Afterwards, we
153 investigated the fault structure and spatiotemporal evolution of the aftershocks (Section
154 3) and extracted information about the generation mechanism of the Yamagata-Oki
155 earthquake and more generally, shallow intraplate earthquakes (Section 4).
156
157

158 ## 2. Data and Methods

159 In this section, we describe the data (subsection 2.1) and methods to detect early
160 aftershocks (subsection 2.2), to relocate hypocenters (subsection 2.3), and to determine
161 focal mechanisms (subsection 2.4) of earthquakes that occurred in the source region of
162 the 2019 Yamagata-Oki earthquake. We also explain the method to estimate the surface
163 strain rate prior to the mainshock by using global navigation satellite system (GNSS) data
164 (subsection 2.5).
165

166 ### 2.1. Data

167 We analyzed 4,255 earthquakes listed in the Japan Meteorological Agency (JMA)
168 unified catalogue from March 1, 2003 to May 10, 2020 (Fig. 2) and the waveforms
169 recorded at the seismic stations surrounding the source region (Fig. S1). For the following
170 waveform analyses (subsection 2.2, 2.3 and 2.4), we constructed P- and S-wave windows
171 starting from 0.3 s before the arrival with the durations of 2.5 s and 4.0 s, respectively,
172 for each earthquake-station pair. For the arrival time, we used manually picked times
173 listed in the JMA unified catalogue, if available; otherwise, we used theoretical arrival
174 times computed by assuming the same velocity model as used in the JMA unified
175 catalogue. Moreover, we used the daily location data at the national GNSS network called
176 GEONET (GNSS Earth Observation Network System;
177 https://www.gsi.go.jp/ENGLISH/index.html) (Fig. S1) provided by the Geospatial
178 Information Authority of Japan (GSI) to estimate the strain rate (subsection 2.5).
179

180 ### 2.2. Detection of early aftershocks

181 The minimum magnitude of completeness temporally increases for a certain period
182 immediately after a large earthquake. To obtain a comprehensive view of the
183 spatiotemporal evolution of the aftershocks of the 2019 Yamagata-Oki earthquake, we

184 performed early aftershock detection to identify the undetected earthquakes in the JMA
185 unified catalogue. In the first step, we used the waveform data obtained at the two nearest
186 stations to identify the possible events, which are not detected in the JMA unified
187 catalogue. In the second step, we used the waveform data obtained at a large number of
188 stations to verify that the identified events are earthquakes in the source region.

189 We first applied the template matching method (Schaff and Waldhauser, 2010) to
190 the continuous waveform data obtained at the two nearest stations (YATSUM and
191 AWASHI shown by purple inverted triangles in Fig. S1) from the source region from June
192 18 to June 19, 2019 (JST). We followed the procedure outlined in Yoshida and Hasegawa
193 (2018a) modified after Shelly et al. (2013). We used 4,255 earthquakes in the JMA unified
194 catalogue (referred to as JMA events) as template events. We applied a bandpass filter
195 with a passband frequency of 5–12 Hz to the continuous waveforms and the S-wave
196 windows of the JMA events and then downsampled the waveforms to 25 samples per
197 second.

198 We compared the S-wave windows of the template events (duration of 4.0 s) with
199 the continuous waveform data; we calculated the correlation coefficients cc_i (the i-th
200 point) on each waveform at each time lag (incremented at 0.04 s intervals), We computed
201 the time series of $cc_i' = \max(cc_{i-1}, cc_i, cc_{i+1})$, and obtained the sum of cc_i' over all
202 the stations and components (CC_i). We computed the median value and the median
203 absolute deviation (MAD) of CC_i for the day. If CC_i exceeds the median value added
204 by the twelve times of MAD, we regarded it as a possible missing event unless it is listed
205 in the JMA unified catalogue. Consequently, we newly obtained 1,207 possible events.

206 Signals of certain newly-detected events were too small to evaluate whether they
207 corresponded to the waveforms of earthquakes in the source region. As the second step,
208 we compared the waveforms of the possible events with those of the JMA events at a
209 large number of stations (46 green triangles in Fig. S1) to eliminate such uncertain events.
210 For each possible event, we constructed the P-wave and S-wave windows in the same
211 way as for the JMA events (durations of 2.5 s for P-wave and 4.0 s for S-wave starting at
212 0.3 s before their onsets). The onset timing is assumed to be the same as that of the most
213 correlated JMA event during the detection. We evaluated the waveform similarity
214 between each newly-detected event and JMA event at each station and component; when
215 a newly-detected event did not satisfy the waveform similarity threshold for five or more
216 JMA events, we eliminated that event. The threshold of the waveform similarity is 0.8 in
217 cross-correlation coefficients for the P- and/or S-wave windows at more than two stations.
218 Consequently, we eliminated 829 events and obtained 378 new events (Fig. 3c). Thus, we

created our earthquake catalogue, which consists of 4,556 earthquakes in total.

We determined the magnitudes of the newly-detected events based on the relative waveform amplitudes of P- and S-waves to those of JMA events. We assumed that the JMA magnitude is equal to the moment magnitude (Hanks and Kanamori, 1979) and the ratio of the waveform amplitude is equal to the ratio of the seismic moment when the station is the same and the sources have similar focal mechanisms and locations. We first aligned the timings of the waveforms by using the lag time of each waveform pair with high similarity (cc $\geq$0.8). The waveform similarity ensures similarity in the source mechanism and location. Afterwards, we compared the amplitudes of the waveform pairs at each time, applied principal component analysis (PCA), and obtained the best amplitude ratio of the waveform pair (Yoshida et al., 2019b). We obtained the amplitude ratios of a detected event with various JMA events at various seismic stations and determined the seismic moment of the detected event as the mean value weighted by the cross-correlation coefficient. We finally determined the magnitude of the detected events by using the relationship between the seismic moment and the moment magnitude (Hanks and Kanamori, 1979).

2.3. Hypocenter relocation

We relocated the hypocenters of earthquakes from our earthquake catalogue obtained in subsection 2.2 using the double-difference method (Waldhauser and Ellsworth, 2000) following the procedure outlined in Yoshida and Hasegawa (2018a). We first extracted the P-wave (101,611) and S-wave (131,760) differential arrival time data from the JMA unified catalog. We also used the waveform data obtained at stations close to the source area (Fig. S1a) for the waveform correlation measurements of differential arrival times. These stations are operated by Tohoku University, JMA, and NIED Hi-net (National Research Institute for Earth Science and Disaster Resilience, 2019a) where three-component velocity-type seismograms are recorded at a sampling rate of 100 Hz. We applied a bandpass filter with frequencies ranging between 5 and 12 Hz and computed the cross-correlation function. Differential arrival times derived from the cross-correlation function were used for the relocation if the cross-correlation coefficient was higher than 0.8. The size of the differential arrival time data for P- and S-waves, derived from the waveform cross-correlation delay measurements, was 650,500 and 810,036, respectively.

We applied the double-difference earthquake relocation method (Waldhauser and

253 Ellsworth, 2000) to the differential arrival time data. We assumed the 1-D velocity model
254 of Hasegawa et al. (1978), which was routinely used at Tohoku University to determine
255 the hypocenter locations and focal mechanisms of the events in northeast Japan. We
256 evaluated the uncertainty in the relative hypocenter locations by recalculating the
257 hypocenters 1,000 times, based on bootstrap resampling of differential arrival time data.

258

259 **2.4. Determination of focal mechanisms**

260 To determine the focal mechanisms, we used the relative amplitudes of direct P-
261 and S-waves corrected by those of a reference earthquake whose focal mechanism was
262 already determined. We followed the procedure outlined in Yoshida et al. (2019b), which
263 utilizes the amplitude ratios of P-, SH-, and SV-waves by assuming that the medium in
264 the vicinity of the source is homogeneous and isotropic (Dahm, 1996). We restricted the
265 distance between the target and reference events to less than 3 km to reduce the
266 differences in the propagation and site effects. We used the waveform correlation between
267 the target and reference earthquakes to reliably obtain the amplitude ratio data.

268 We adopted twelve focal mechanisms listed in the JMA unified catalogue (Fig. 2b)
269 as reference focal mechanisms using the P-wave first-motion polarity data. We applied a
270 bandpass filter with frequency of 2–5 Hz to both the P-wave and S-wave windows. The
271 amplitude ratio was computed at each seismic station using the same method described
272 in subsection 2.1, when the cross-correlation coefficient is greater than 0.75 between the
273 waveforms of the target event and the reference event. If the amplitude ratio data were
274 obtained from more than eight different seismic stations and 15 channels, we estimated
275 the moment tensor components. We computed 2,000 focal mechanisms for each target
276 event based on the bootstrap resampling of the amplitude ratio data. The difference in the
277 focal mechanisms from the best solution was measured by the 3-D rotation angle (Kagan,
278 1991). If the 90% confidence interval was larger than 30°, we discarded the result. If focal
279 mechanism of one target event was obtained from different reference events, we adopted
280 the one with the minimum confidence interval.

281

282 **2.5. Estimation of strain rate prior to the mainshock**

283 We estimated the temporal changes in the surface strain rate prior to 2019
284 Yamagata-Oki earthquake by using the location data at the national GNSS network
285 GEONET. We estimated the spatial distribution of surface strain rates in the following
286 periods: (1) March 9, 2009 to March 10, 2011 (before the 2011 Tohoku-Oki earthquake),

(2) March 12, 2011 to June 18, 2014 (after the coseismic change of the 2011 Tohoku-Oki earthquake), (3) June 19, 2014 to June 18, 2018, and (4) June 19, 2018 to June 18, 2019 (before the 2019 Yamagata-Oki earthquake).

We used the routine daily coordinate solutions (F3 solutions) provided by the GSI obtained at the GEONET stations (Fig. S1). We applied the method by Shen et al. (1996) to the mean displacement rates during these periods and obtained the spatial distribution of the strain rate at each 0.05°-spaced grid node.

3. Results

3.1. Fault Structure

We obtained the relocated hypocenters of 4,501 events and determined the focal mechanisms for 269 events. Location data for 55 earthquakes were removed because their hypocenters were located above the ground surface (49 JMA events and six newly-detected events). We computed the differences between the maximum and minimum values in the 95% confidence interval of the hypocenter locations (Fig. S2) and obtained the medians as a measure of estimation error: 0.0014° in longitude, 0.0013° in latitude, and 0.22 km in depth for the JMA events and 0.0021° in longitude, 0.0017° in latitude, and 0.33 km in depth for the newly-detected events.

The present hypocenter relocation succeeded in delineating a few planar structures of hypocenters (Fig. 4) from the scattered distribution of the initial hypocenters of the JMA unified catalog (Fig. 2). Such drastic changes in the hypocenter distribution were also obtained for other earthquake clusters in northeast Japan based on a similar relocation method by using numerous and precise differential arrival time data (Yoshida and Hasegawa, 2018a and b, Yoshida et al., 2020). The largest plane of aftershock hypocenters is the one dipping eastward approximately 15 km long and 10 km wide (gray rectangle in Fig. 4a and gray lines in Figs. 4c–i), at the bottom of which the mainshock hypocenter is located. We also observed two west-dipping conjugate planes in the southern part (green rectangle and green lines) and the shallower part (black rectangle and red lines) of the aftershock area.

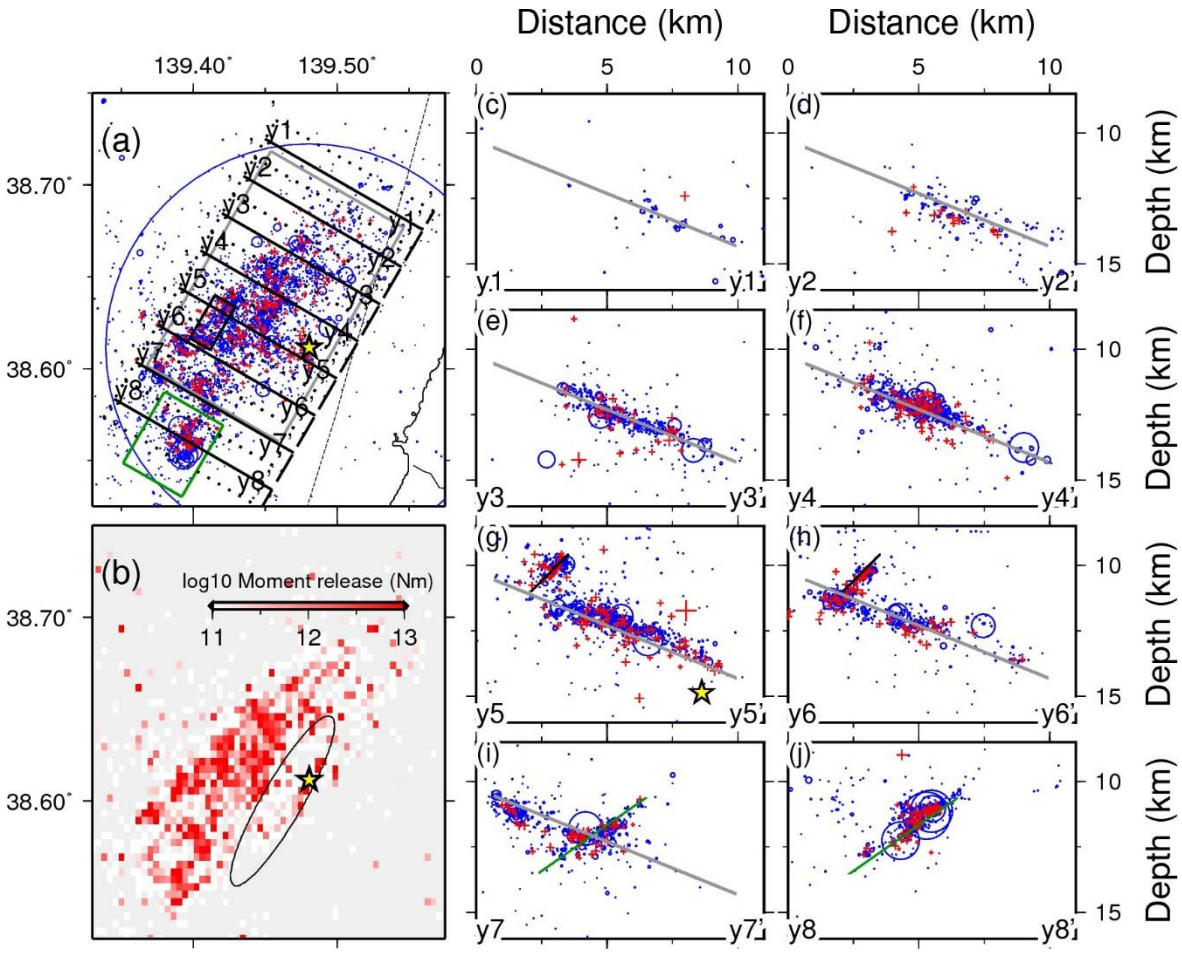

Fig. 4. Distribution of the relocated hypocenters. (a) A map view showing the focal region of the 2019 Yamagata-Oki earthquake. Blue circles represent the hypocenters. The size of each circle corresponds to the diameter of the fault, assuming a stress drop of 3 MPa. The star denotes the hypocenter of the mainshock. Gray, green, and red rectangles denote the model fault planes. Red crosses indicate the hypocenters of the newly-detected events. The sizes of the crosses are ten times as large as those of the JMA events in order to clearly show their distribution. (b) The moment release amount of the aftershocks computed at each 0.04°-spaced grid-cel is shown by the color scale. The black ellipse shows the seismic gap. (c)–(j) Cross-sectional views of the vertical hypocenter distribution along the lines indicated in (a). Gray, green, and black lines denote the model fault planes.

Earthquakes in and around the aftershock area before the mainshock (Figs. 5a and b) also appear to have occurred along the same fault structures as aftershocks. Some

earthquakes were located near the hypocenter of the mainshock, but most were located on the western segments of the fault structure of aftershocks (Figs. 5c and d).

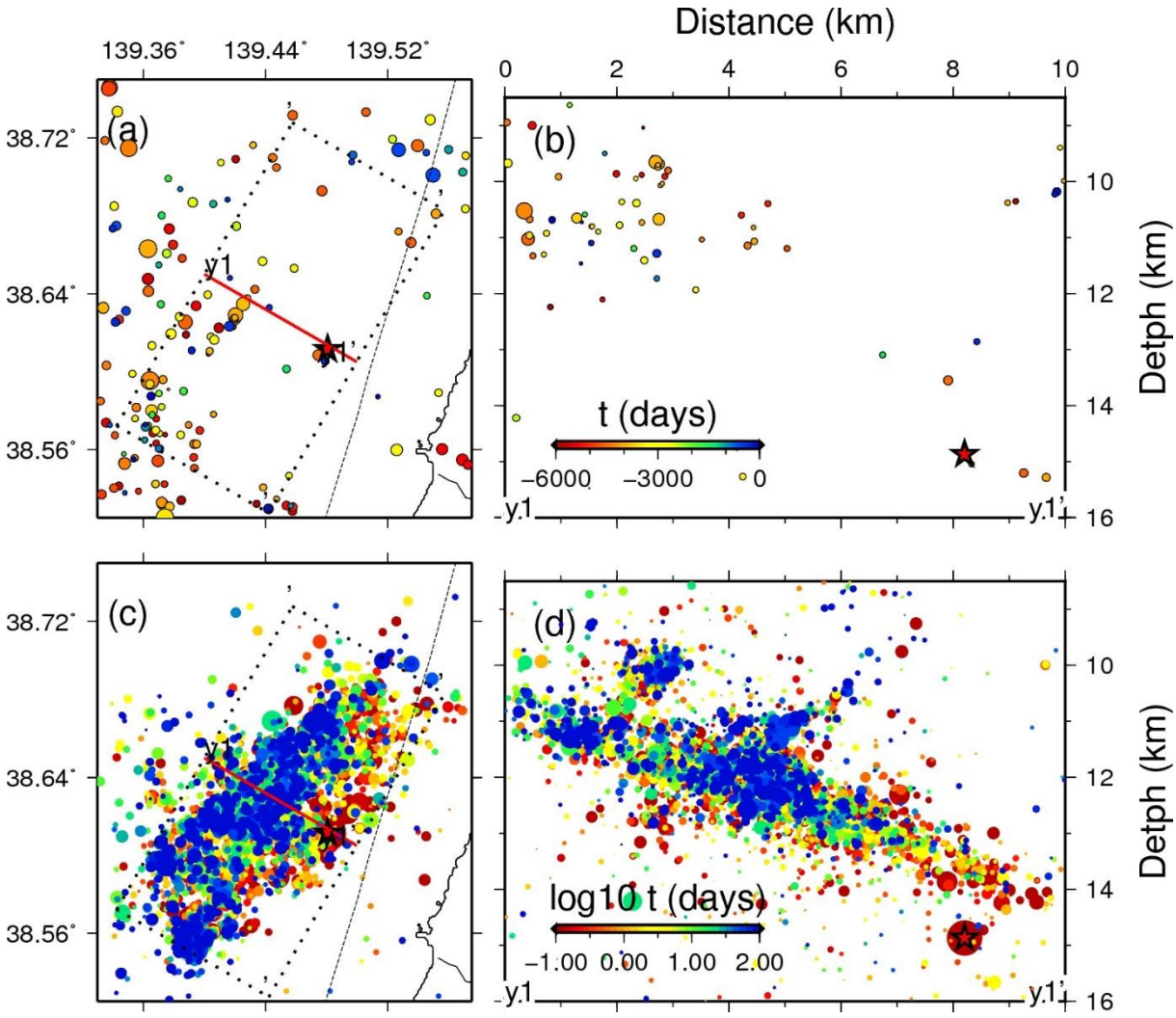

Fig. 5. Spatiotemporal distribution of earthquakes. The occurrence times measured from the mainshock are shown in the color scale in (a), (c) map-view and (b), (d) cross-sectional view within the range shown by the broken rectangle in (a) and (c). (a), (b): before the mainshock. (c), (d): after the mainshock. The star indicates the mainshock.

Figure 6 shows the spatial distribution of the focal mechanisms determined in this

study and by the JMA before and after the Yamagata-Oki earthquake. Most of them have WNW–ESE compressional reverse-fault focal mechanisms similar to that of the mainshock. Most of those aftershocks have nodal planes nearly parallel to the alignments of the hypocenters, suggesting that individual aftershocks occur on the macroscopic planar structures illustrated by the hypocenters.

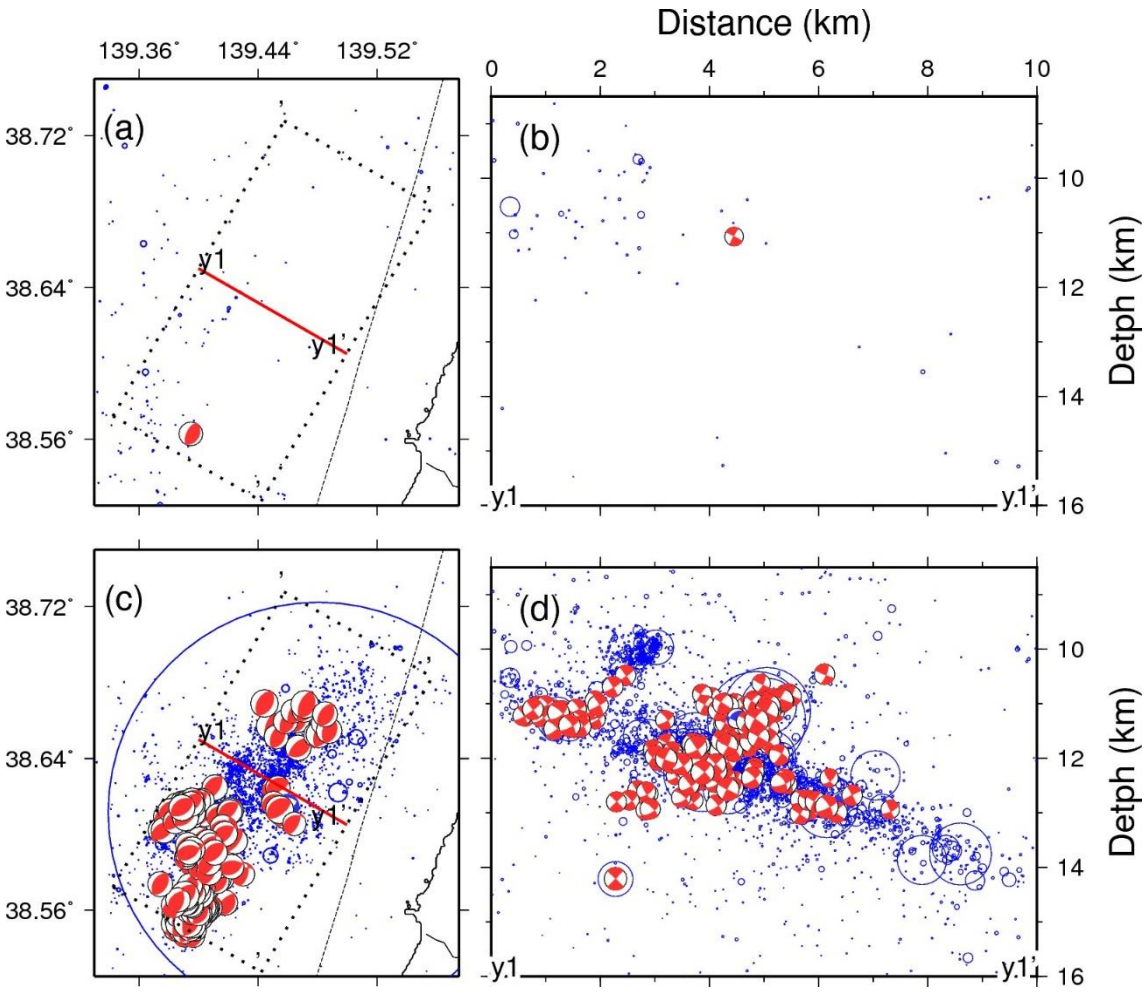

Fig. 6 (a), (b) Distribution of the focal mechanisms of aftershocks. Focal mechanisms are shown by the beach ball in (a), (c) map-view and (b), (d) cross-sectional view within the range shown by the broken rectangle in (a) and (c). (a), (b): before the mainshock. (c), (d): after the mainshock. Blue circles indicate the locations of relocated hypocenters.

3.2. Seismic gap of earthquakes before and after the mainshock

Aftershocks did not occur in the area up to 2–3 km from the mainshock hypocenter along

the east-dipping fault plane (z = 12.5–15.0 km in Figs. 4f–h). Intensive aftershock activities occurred in the shallower portions above this seismic gap along the east-dipping plane (z = 10.0–12.5 km) and along two conjugate planes. A seismic gap of aftershocks formed at a deeper portion of the aftershock area and along the shallower side of the mainshock hypocenter along the east-dipping fault plane. In this area, earthquakes did not occur before the mainshock.

To analyze this tendency differently, we computed the seismic moment release amount of each earthquake by assuming that the magnitude is equal to the moment magnitude. Then, we summed the moment release amount rate at each evenly-spaced point every 0.04° by using the aftershocks within the nearest grid-cell (Fig. 4 (b)). The moment release amount of aftershocks and earthquakes before the mainshock is smaller ($< 10^{11} - 10^{12}$ Nm) in the region up to 2–3 km from the mainshock hypocenter along the east-dipping fault plane, corresponding to the seismic gap, than the other regions in its shallower extension ($\sim 10^{13}$ Nm).

3.3. Migration and expansion of the aftershock distribution

The aftershock area appears to expand with time (Figs. 5c and d). Fig. 7 shows the spatiotemporal evolution of the aftershock distribution in four periods: (a), (b) 0 to 0.2 d, (c), (d) 0.2 to 2 d, (e), (f) 2 to 30 d, and (g), (h) 30 to 300 d from the mainshock. Hypocenters tend to be located in the deeper portion in the earlier period (Figs. 7a and b) but expand to the shallower part in the later periods (Figs. 7c through d). Fig. 8 shows the direct comparison of the occurrence times of aftershocks with depth, longitude, and latitude. We sorted the earthquakes by time and divided them into 45 bins with 100 events. We computed the two levels above or below where 10% of the events are contained in each bin and showed the levels in Fig. 8. The aftershock hypocenters moved toward the shallower part approximately following the logarithm of time (Figs. 8a and b). Aftershocks in the deeper portion of the fault (z >13 km) intensively occurred in the first day from the mainshock but ceased after ~1 d from the mainshock (Fig. 8a).

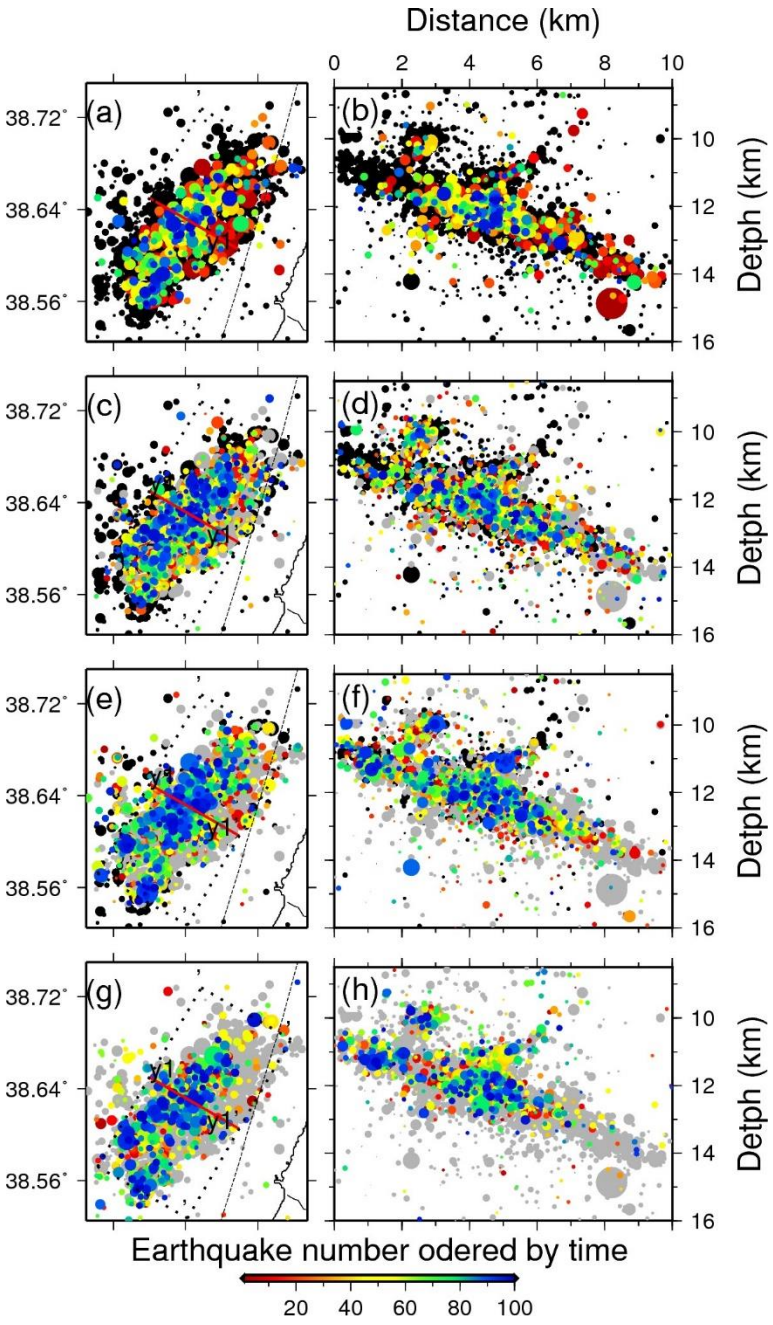

Fig. 7 Spatiotemporal distribution of earthquakes for four periods: (a), (b) 0 to 0.2 d, (c), (d) 0.2 to 2 d, (e), (f) 2 to 30 d, and (g), (h) 30 to 300 d from the mainshock. The color scale in shows the relative number of earthquakes ordered by time from the beginning to the end of the periods. (a), (c), (e), (g): map-view; (b), (d), (f), (h): cross-sectional view within the range shown by the broken rectangle in (a), (c), (e) and (g). Gray and black circles show the location of earthquakes before and after these periods, respectively.

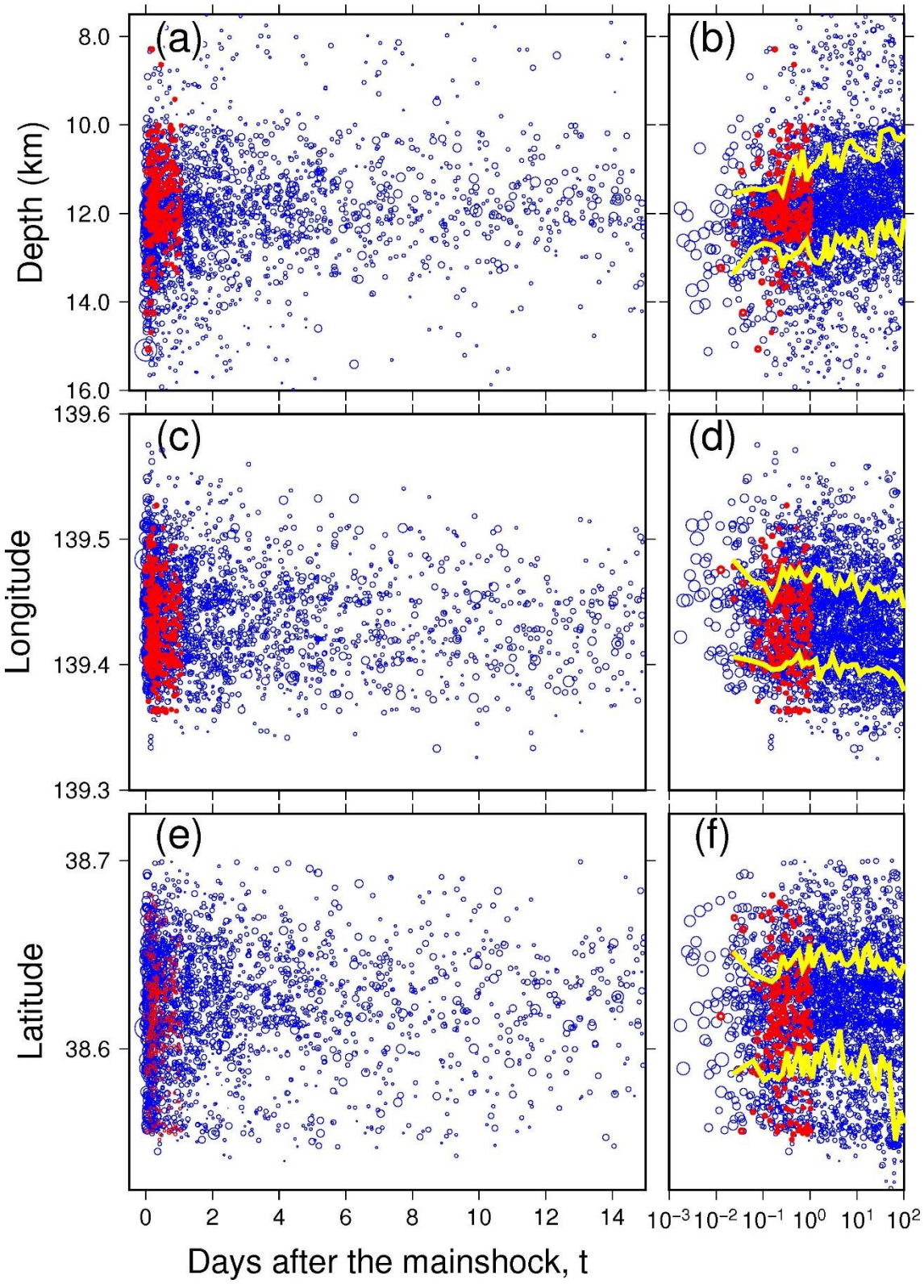
(a)
(b)
(c)
(d)
(e)
(f)
Depth (km)
8.0
10.0
12.0
14.0
16.0
Longitude
139.6
139.5
139.4
139.3
Latitude
38.7
38.6
0
2
4
6
8
10
12
14
10^{-3} 10^{-2} 10^{-1} 10^{0} 10^{1} 10^{2}
Days after the mainshock, t

406 **Fig. 8** Spatiotemporal distribution of aftershocks. (a), (b): depth, (c), (d): longitude,
407 and (e), (f): latitude. Blue and red circles show the events taken from the JMA unified
408 catalogue and those detected in this study, respectively. Occurrence times are shown
409 in the linear scale in (a), (c), and (e) and in the logarithmic scale in (b), (d), and (f).
410 Yellow curves in (b), (c), and (d) show the levels above and below where 10% of the
411 events are contained in each bin with 100 events sorted by time.
412
413 **3.4. Strain rate prior to the mainshock**
414 Fig. 9 shows the spatial distribution of the strain rate for four periods: (a) March 9,
415 2009 to March 10, 2011 (before the 2011 Tohoku-Oki earthquake), (b) March 12, 2011
416 (after the coseismic change of the 2011 Tohoku-Oki earthquake) to June 18, 2014, (c)
417 June 19, 2014 to June 18, 2018, and (d) June 19, 2018 to June 18, 2019 (before the 2019
418 Yamagata-Oki earthquake).
419 Northeast Japan including the source region of the Yamagata-Oki earthquake was
420 characterized by the E–W contraction strain rate before the 2011 Tohoku-Oki earthquake
421 (Fig. 9a), which is consistent with the results of the previous studies (Sagiya et al., 2000;
422 Yoshida et al., 2015). However, the 2011 Tohoku-Oki earthquake drastically changed the
423 spatial distribution of the strain rate, and the east-west extension strain rate spread all over
424 the region (Fig. 9b). This E–W extension continued near the source region of the
425 Yamagata-Oki earthquake after the Tohoku-Oki earthquake (Fig. 9c) because of the
426 postseismic deformation such as the afterslip (Ozawa et al., 2011) along the plate interface
427 and the viscoelastic response of the mantle (Hu et al., 2016). The E–W extension strain
428 rate further continued until the occurrence of the Yamagata-Oki earthquake, as shown in
429 the strain rate map for the latest period (from June 19, 2018 to June 18, 2019), which was
430 just before the Yamagata-Oki earthquake.

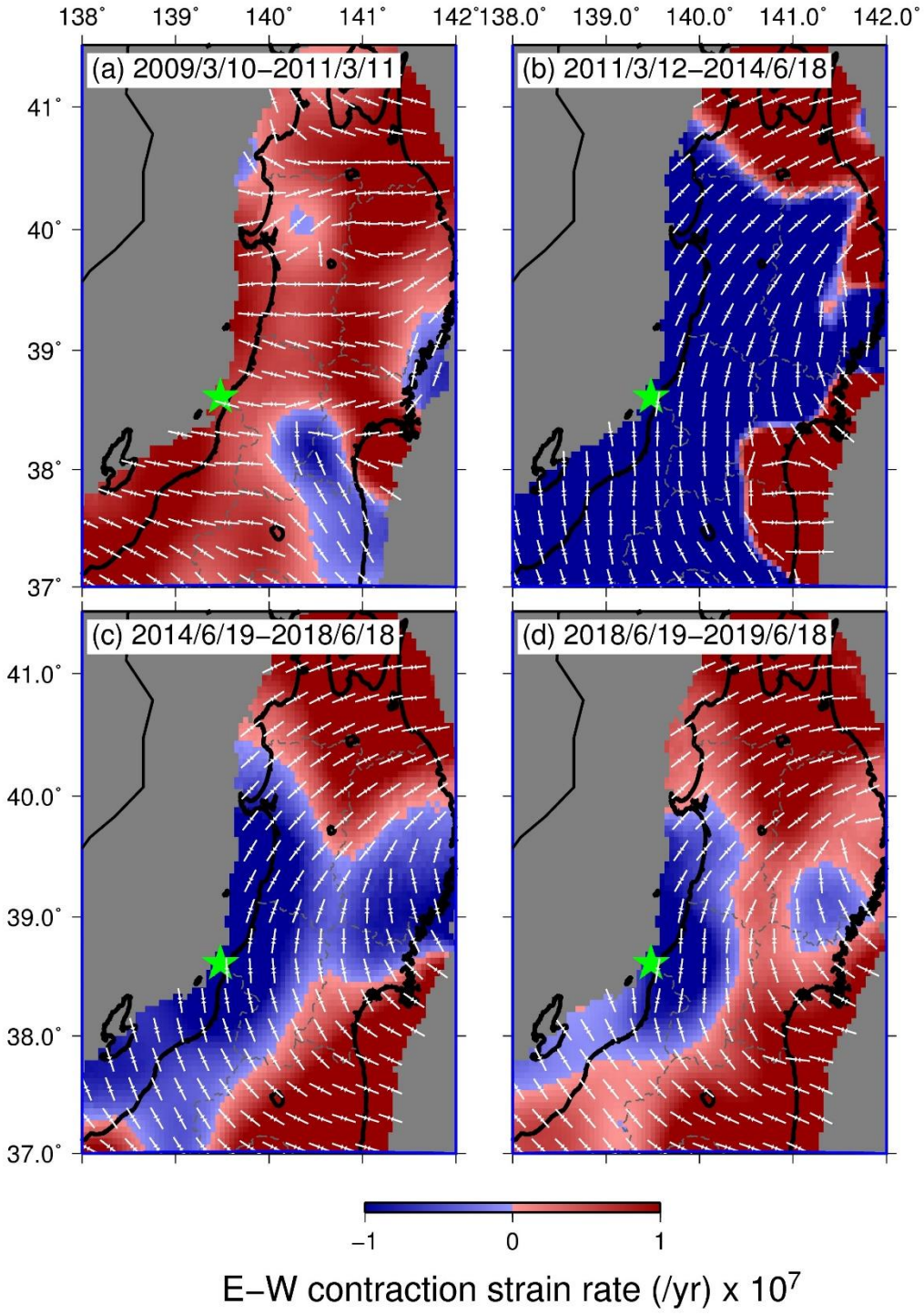

Fig. 9. Spatial distribution of the strain rate in northeast Japan obtained from GEONET data for four periods prior to the 2019 Yamagata-Oki earthquake: (a)

March 9, 2009 to March 10, 2011 (before the 2011 Tohoku-Oki earthquake), (b) March 12, 2011 (after the coseismic change of the 2011 Tohoku-Oki earthquake) to June 18, 2014, (c) June 19, 2014 to June 18, 2018, and (d) June 19, 2018 to June 18, 2019 (before the 2019 Yamagata-Oki earthquake). The E–W contraction rate is shown by the color scale. The bars denote principal contraction strain rate axes. The star indicates the location of the Yamagata-Oki earthquake.

There are two GNSS stations near the source region of the Yamagata-Oki earthquake (blue crosses in Fig. S1), one of which is located west of the source region and the other east. Fig. 10 shows the temporal changes in the distance in the E–W direction between these stations. The E–W distance between the two stations continued to increase after the 2011 Tohoku-Oki earthquake, suggesting that the E–W extension continued even before the Yamagata-Oki earthquake.

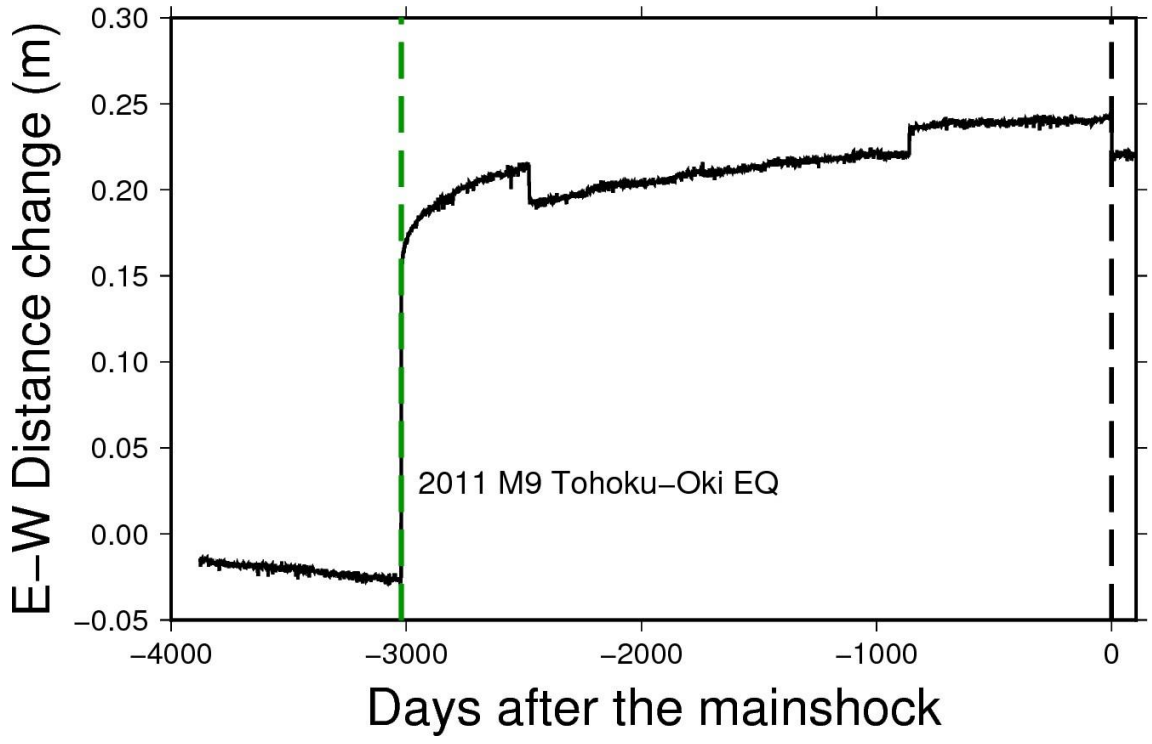

Fig. 10. Distance change in the E–W direction between the two GPS stations (1162 and 0231; blue crosses in Fig. S1) near the source region of the 2019 Yamagata-Oki earthquake from Jan. 1, 2007 to Sep. 30, 2019. The positive sign indicates the

increase in the distance between the two stations.

4. Discussion

4.1. Occurrence mechanism of the 2019 Yamagata-Oki earthquake in the stress shadow

The 2019 M6.7 Yamagata-Oki earthquake occurred in the coseismic stress shadow of the 2011 M9.0 Tohoku-Oki earthquake. The seismicity rate in the source region of the Yamagata-Oki earthquake decreased after the Tohoku-Oki earthquake in agreement with the stress shadow (Fig. 3b). The source region was located in the E–W extension and north–south contraction strain rate field even immediately before the Yamagata-Oki earthquake (Fig. 9d). The occurrence of the Yamagata-Oki earthquake with the east-west compressional reverse-faulting mechanism in this situation provides important constraints for the occurrence mechanism; thus, the occurrence of this earthquake is related to the local effects on the stress and/or fault strength.

We observed an upward migration of aftershocks of the 2019 Yamagata-Oki earthquake (Fig. 8b). Similar upward migrations were also observed for several earthquake swarms triggered in the central part of northeast Japan after the 2011 Tohoku-Oki earthquake (Okada et al., 2015; Yoshida and Hasegawa, 2018a, b). Those earthquake swarms occurred in the stress shadow of the 2011 Tohoku-Oki earthquake as well and were caused by the increase in pore pressure after the 2011 earthquake (Terakawa et al., 2013; Yoshida et al., 2016, 2017). The upward migration of the aftershocks of the Yamagata-Oki earthquake to the outside of the three main planes ($z < 10$ km in Figs. 7 and 8) can be explained by the upward fluid discharge after the earthquake. By considering the involvement of fluids, we can also explain the occurrence of the mainshock in the stress shadow because the increase in pore fluid pressure reduces the fault strength.

Aftershock migration can be explained by the effects other than the pore pressure migration, such as postseismic slip propagation (Wesson, 1987; Kato, 2004; Hsu et al., 2006; Kato et al., 2007; Peng and Zhao, 2009; Frank et al., 2017; Perfettini et al., 2018; Yoshida et al., 2020) and aftershock-to-aftershock interactions (Helmstetter, 2002). By adopting these models, we may explain the observed upward aftershock migration without pore pressure migration. The expansion of the aftershock region with the logarithm of time observed in this study (Fig. 8b) is consistent with the observations and simulations of the post-seismic slip (Kato et al., 2007; Peng and Zhao, 2009; Perfettini et al., 2018). However, even if these stress triggering models are adopted as the cause of the

491 expansion of the aftershock region, the mainshock occurrence in the stress shadow should
492 still be explained independently. We also need to explain the occurrence of the M6.7 E–
493 W compressional reverse-faulting earthquake in the field with the increased E–W
494 extensional strain rate. One possible explanation is based on the localized deformation in
495 the deeper part; if aseismic slips proceed in the deeper extension of the fault, they may
496 locally increase the shear stress on the fault and cause an earthquake even in the
497 macroscopic stress shadow of the Tohoku-Oki earthquake. Meneses-Gutierrez and Sagiya
498 (2016) recently analyzed the surface deformation in the Niigata-Kobe Tectonic Zone
499 (NKTZ), which is also located in the stress shadow of the 2011 Tohoku-Oki earthquake.
500 They found a localized contraction zone around the northern part of the NKTZ both
501 before and after the Tohoku-Oki earthquake and explained this observation by a persistent
502 aseismic creep in the deeper portion of the fault. Aseismic creeps may decelerate when
503 the shear stress magnitude decreases but may not completely cease. Previous studies
504 suggested that the active deformation zone along the eastern margin of the Japan Sea is
505 the northern extension of the NKTZ (Nakamura, 1983). However, it is not likely that such
506 a deeper deformation alone, which probably slowed down after the 2011 earthquake if
507 existed, increased the shear stress to exceed the level just before the 2011 Tohoku-Oki
508 earthquake and caused the mainshock rupture of the 2017 Yamagata-Oki earthquake. In
509 fact, we did not observe an east-west contraction between the two nearest GNSS stations
510 before the Yamagata-Oki earthquake (Fig. 10b).
511 Thus, we preferred the pore pressure migration model to explain the occurrence of
512 the 2019 Yamagata-Oki earthquake. Pore pressure increase may also promote localized
513 deformation beneath the fault zone. It may reduce the strength of the deeper extension
514 part of the fault and accelerate creeps on it, even triggering aseismic slip events. It is
515 possible that ore pressure migration and localized deformation in the deeper part of the
516 fault may have coexisted and contributed to the occurrence of the 2019 Yamagata-Oki
517 earthquake. The propagation of the postseismic slip and the aftershock-to-aftershock
518 interaction may also have contributed to the aftershock migration together with the pore
519 pressure migration.
520 Seismic tomography results suggest that a low-velocity zone in the mantle wedge
521 extends westward from beneath the volcanic front to beneath the Japan Sea (Zhao et al.,
522 2011). The low-velocity zone is considered to represent the ascending flow portion of the
523 secondary convection within the mantle wedge and therefore contains fluids dehydrated
524 from the slab and resultant melts (Hasegawa and Nakajima, 2004). Fluids released from
525 the mantle diapirs rising from this low-velocity zone in the mantle wedge may reach
526 beneath the focal region of the 2019 Yamagata-Oki earthquake. They may also contribute

to the formation of the active deformation zone along the eastern margin of the Japan Sea.

The involvement of fluids has been more often reported for earthquake swarms (Parotidis et al., 2005; Yukutake et al., 2011; Shelly et al., 2013) but has also been considered for mainshock-aftershock sequences (Nur and Booker, 1972; Yamashita and Knopoff, 1987; Sibson, 1992). In fact, the differential stress magnitude in northeast Japan is estimated to be too small (a few tens of MPa) to cause earthquakes without the reduction in fault strength (Yoshida et al., 2014, 2015a, 2015b, and 2016). The present observations support the hypothesis that the involvement of fluids plays an important role in the occurrence of the mainshock-aftershock sequences. Recently, Matsumoto et al. (2020) examined the foreshocks and aftershocks of the 2017 M5.3 Kagoshima Bay earthquake and reached a similar conclusion that the foreshock-mainshock-aftershock sequences were caused by the fluid movements. They found that foreshock hypocenters migrated along the mainshock fault plane and that aftershock hypocenters migrated upward similarly to the present observations. In the fault-valve model of Sibson (1992), uprising fluids originated from the deeper portion reduced the fault strength, caused the earthquake, and discharged further upward. This model accounts for the newly observed features of the 2019 Yamagata-Oki earthquake; i.e., its occurrence in the stress shadow and the upward migration of aftershock hypocenters.

4.2. Seismic gap as a clue to estimate the large coseismic slip region of the mainshock

We delineated three planar structures of hypocenters (Fig. 4). The mainshock hypocenter is located at the deepest edge of the east-dipping plane of the hypocenters distribution, which likely represents the mainshock fault plane.

The seismic gap of aftershocks near the mainshock hypocenter (the ellipse in Fig. 4b) likely represents a large coseismic slip area of the mainshock (Figs. 4a and b). A large amount of shear stress may have been released in the area with the large coseismic slip of the mainshock, which may be the reason the aftershocks did not occur there. Previous studies reported a spatial separation between the mainshock coseismic slip area and the areas where aftershocks are active based on the direct comparison of aftershock distribution and coseismic slip distribution (Mendoza and Hartzell, 1988; Das and Henry, 2003; Woessner et al., 2006; Asano et al., 2011; Ebel and Chambers, 2016; Yoshida et al., 2016; Yoshida et al., 2016 and 2020; Ross et al., 2017b, 2018; Wetzler et al., 2018). The spatial separation can be attributed to the differences in the frictional properties along the fault.

4. Conclusions

In this study, we investigated the fault structure and spatiotemporal variations of the aftershocks of the 2019 M6.7 Yamagata-Oki earthquake, which occurred in the stress shadow of the 2011 M9.0 Tohoku-Oki earthquake, to understand the occurrence mechanisms of earthquake sequences. Additionally, we investigated the spatiotemporal evolution of horizontal strain rates before the occurrence of the mainshock.

Precisely relocated aftershock hypocenters formed three planar structures. One of the two nodal planes of focal mechanisms of each event were almost parallel to the hypocenter alignments, suggesting that individual aftershocks were mainly caused by afterslip along the faults delineated by the aftershocks. A seismic gap of aftershocks existed near the mainshock hypocenter on the major east-dipping plane may reflect the area with large coseismic slip of the mainshock. Aftershock hypocenters rapidly migrated upward from the deeper part of the fault similar to the recent earthquake swarm sequences triggered after the 2011 Tohoku-Oki earthquake in the stress shadow.

The spatial distribution of the surface strain rate in northeast Japan, including the source region of the 2019 Yamagata-Oki earthquake, was characterized by E–W contraction strain rate; however, the 2011 Tohoku-Oki earthquake drastically changed the spatial distribution and the E–W extension strain rate spread over northeast Japan. Near the source region of the Yamagata-Oki earthquake, this E–W extension strain rate progressed until the occurrence of the mainshock due to the postseismic deformation.

The observed upward hypocenter migrations, together with the earthquake occurrence in the stress shadow and in the E–W extension strain rate field, suggest that the Yamagata-Oki earthquake was caused by the reduction in the fault strength due to the rising crustal fluids from the deep part. Moreover, the existence of fluids may promote aseismic deformations in the deeper part of the fault. Localized aseismic deformations beneath the fault may have contributed to the occurrence of this earthquake and the formation of the active deformation zone along the eastern margin of the Japan Sea.

In this study, we constrained the occurrence mechanism of the 2019 Yamagata-Oki earthquake by considering the occurrence of earthquake in the stress shadow. Fluid migrations likely contribute to the occurrence of more earthquakes. Aseismic processes, including pore pressure migrations and localized aseismic deformations, in the deeper part of the fault play important roles in the occurrence of increased shallow intraplate earthquakes.

Acknowledgement

This study used hypocenters and P-and S-wave arrival time data reported in the unified catalog of the JMA (https://www.data.jma.go.jp/svd/eqev/data/bulletin/index_e.html).

The seismograms were collected and stored by JMA, national universities, and National Research Institute for Earth Science and Disaster Resilience (http://www.hinet.bosai.go.jp/?LANG=en). The figures in this paper were created using GMT (Wessel and Smith, 1998). This research was supported by JSPS KAKENHI Grant Number JP 17K1437 and 17H05309.

606 **References**

607 Bird, P., 2003. An updated digital model of plate boundaries. Geochemistry Geophys.
608 Geosystems 4. https://doi.org/10.1029/2001GC000252
609 Dahm, T., 1996. Relative moment tensor inversion based on ray theory: Theory and
610 synthetic tests. Geophys. J. Int. 124, 245–257. https://doi.org/10.1111/j.1365-
611 246X.1996.tb06368.x
612 Das, S., Henry, C., 2003. Spatial relation between main earthquake slip and its aftershock
613 distribution. Rev. Geophys. 41. https://doi.org/10.1029/2002RG000119
614 Ebel, J.E., Chambers, D.W., 2016. Using the locations of M ≥ 4 earthquakes to delineate
615 the extents of the ruptures of past major earthquakes. Geophys. J. Int. 207, 862–
616 875. https://doi.org/10.1093/gji/ggw312
617 Fukuyama, E., Ishida, M., Dreger, D.S., Kawai, H., 1998. Automated seismic moment
618 tensor determination by using on-line broadband seismic waveforms. Jishin 51,
619 149–156.
620 Hanks, T.C., Kanamori, H., 1979. A moment magnitude scale, in: Journal of Geophysical
621 Research B: Solid Earth. pp. 2348–2350.
622 https://doi.org/10.1029/JB084iB05p02348
623 Hasegawa, A., Nakajima, J., Umino, N., Miura, S., 2005. Deep structure of the
624 northeastern Japan arc and its implications for crustal deformation and shallow
625 seismic activity. Tectonophysics 403, 59–75.
626 https://doi.org/10.1016/j.tecto.2005.03.018
627 Hasegawa, A., Nakajima, J., 2004. Geophysical constraints on slab subduction and arc
628 magmatism, in: Sparks, R.S.J. & Hawkesworth, C.J. (Ed.), Geophysical
629 Monograph Series. AGU, pp. 81–93. https://doi.org/10.1029/150GM08
630 Hasegawa, A., Umino, N., Takagi, A., 1978. Double-planed structure of the deep seismic
631 zone in the northeastern Japan arc. Tectonophysics 47, 43–58.
632 https://doi.org/10.1016/0040-1951(78)90150-6
633 Hasegawa, A., Yoshida, K., Asano, Y., Okada, T., Iinuma, T., Ito, Y., 2012. Change in
634 stress field after the 2011 great Tohoku-Oki earthquake. Earth Planet. Sci. Lett.
635 https://doi.org/10.1016/j.epsl.2012.08.042
636 Heki, K., Miyazaki, S., Takahashi, H., Kasahara, M., Kimata, F., Miura, S., Vasilenko,
637 N.F., Ivashchenko, A., An, K.-D., 1999. The Amurian Plate motion and current
638 plate kinematics in eastern Asia. J. Geophys. Res. Solid Earth 104, 29147–29155.
639 https://doi.org/10.1029/1999JB900295
640 Helmstetter, A., Sornette, D., 2002. Diffusion of epicenters of earthquake aftershocks,
641 Omori's law, and generalized continuous-time random walk models. Phys. Rev. E

642 - Stat. Physics, Plasmas, Fluids, Relat. Interdiscip. Top. 66, 24.
643 https://doi.org/10.1103/PhysRevE.66.061104
644 Hu, Y., Bürgmann, R., Uchida, N., Banerjee, P., Freymueller, J.T., 2016. Stress-driven
645 relaxation of heterogeneous upper mantle and time-dependent afterslip following
646 the 2011 Tohoku earthquake. J. Geophys. Res. Solid Earth 121, 385–411.
647 https://doi.org/10.1002/2015JB012508
648 Iinuma, T., Hino, R., Kido, M., Inazu, D., Osada, Y., Ito, Y., Ohzono, M., Tsushima, H.,
649 Suzuki, S., Fujimoto, H., Miura, S., 2012. Coseismic slip distribution of the 2011
650 off the Pacific Coast of Tohoku Earthquake (M9.0) refined by means of seafloor
651 geodetic data. J. Geophys. Res. Solid Earth 117.
652 https://doi.org/10.1029/2012JB009186
653 Iio, Y., Kobayashi, Y., 2002. A physical understanding of large intraplate earthquakes.
654 Earth, Planets Sp. 54, 1001–1004. https://doi.org/10.1186/BF03353292
655 Kagan, Y.Y., 1991. 3-D rotation of double-couple earthquake sources. Geophys. J. Int.
656 106, 709–716. https://doi.org/10.1111/j.1365-246X.1991.tb06343.x
657 Kato, N., 2004. Interaction of slip on asperities: Numerical simulation of seismic cycles
658 on a two-dimensional planar fault with nonuniform frictional property. J. Geophys.
659 Res. Solid Earth 109, 1–17. https://doi.org/10.1029/2004JB003001
660 Kato, N., 2007. Expansion of aftershock areas caused by propagating post-seismic sliding.
661 Geophys. J. Int. 168, 797–808. https://doi.org/10.1111/j.1365-246X.2006.03255.x
662 Kobayashi, Y., 1983. The start of “subduction” of plate. Earth Mon. 3, 510–518.
663 Liu, L., Zoback, M.D., 1997. Lithospheric strength and intraplate. Tectonics.
664 Matsumoto, Y., Yoshida, K., Hasegawa, A., Matsuzawa, T., 2020. Fault-valve behavior
665 estimated from intensive foreshock and aftershock activity in the 2017 M 5.3
666 Kagoshima Bay, Kyushu, southern Japan, earthquake sequence. Earth Sp. Sci.
667 Open Arch. 30. https://doi.org/10.1002/essoar.10503222.1
668 Mendoza, C., Hartzell, S.H., 1988. Aftershock patterns and main shock faulting. Bull. -
669 Seismol. Soc. Am. 78, 1438–1449.
670 Meneses-Gutierrez, A., Sagiya, T., 2016. Persistent inelastic deformation in central Japan
671 revealed by GPS observation before and after the Tohoku-oki earthquake. Earth
672 Planet. Sci. Lett. 450, 366–371. https://doi.org/10.1016/j.epsl.2016.06.055
673 Nakamura, K., 1983. POSSIBLE NASCENT TRENCH ALONG THE EASTERN
674 JAPAN SEA AS THE CONVERGENT BOUNDARY BETWEEN EURASIAN
675 AND NORTH AMERICAN PLATES. Bull. Earthq. Res. Institute, Univ. Tokyo 58,
676 711–722.
677 National Research Institute for Earth Science and Disaster Resilience (2019). NIED Hi-

678 net. Natl. Res. Inst. Earth Sci. Disaster Resil.,doi:10.17598/NIED.0003
679 Nur, A., Booker, J.R., 1972. Aftershocks caused by pore fluid flow? Science (80-.). 175,
680 885–887. https://doi.org/10.1126/science.175.4024.885
681 Ohtake, M., 1995. A seismic gap in the eastern margin of the Sea of Japan as inferred
682 from the time-space distribution of past seismicity. Isl. Arc 4, 156–165.
683 Okamura, Y., Watanabe, M., Morijiri, R., Satoh, M., 1995. Rifting and basin inversion in
684 the eastern margin of the Japan Sea. Isl. Arc 4, 166–181.
685 https://doi.org/10.1111/j.1440-1738.1995.tb00141.x
686 Ozawa, S., Nishimura, T., Suito, H., Kobayashi, T., Tobita, M., Imakiire, T., 2011.
687 Coseismic and postseismic slip of the 2011 magnitude-9 Tohoku-Oki earthquake.
688 Nature 475, 373–6. https://doi.org/10.1038/nature10227
689 Parotidis, M., Shapiro, S. a., Rothert, E., 2005. Evidence for triggering of the Vogtland
690 swarms 2000 by pore pressure diffusion. J. Geophys. Res. Solid Earth 110, 1–12.
691 https://doi.org/10.1029/2004JB003267
692 Perfettini, H., Frank, W.B., Marsan, D., Bouchon, M., 2018. A Model of Aftershock
693 Migration Driven by Afterslip. Geophys. Res. Lett. 45, 2283–2293.
694 https://doi.org/10.1002/2017GL076287
695 Rice, J.R., 1992. Fault Stress States, Pore Pressure Distributions, and the Weakness of the
696 San Andreas Fault. Fault Mech. Transp. Prop. Rocks.
697 Sagiya, T., Miyazaki, S., Tada, T., 2000. Continuous GPS Array and Present-day Crustal
698 Deformation of Japan. Pure Appl. Geophys. 157, 2303–2322.
699 Shelly, D.R., Moran, S.C., Thelen, W.A., 2013. Evidence for fluid-triggered slip in the
700 2009 Mount Rainier, Washington earthquake swarm. Geophys. Res. Lett. 40, 1506–
701 1512. https://doi.org/10.1002/grl.50354
702 Sibson, R., 1992. Implications of fault-valve behaviour for rupture nucleation and
703 recurrence. Tectonophysics 211, 283–293. https://doi.org/10.1016/0040-
704 1951(92)90065-E
705 Terakawa, T., Hashimoto, C., Matsu'ura, M., 2013. Changes in seismic activity following
706 the 2011 Tohoku-oki earthquake: Effects of pore fluid pressure. Earth Planet. Sci.
707 Lett. 365, 17–24. https://doi.org/10.1016/j.epsl.2013.01.017
708 Waldhauser, F., Ellsworth, W.L., 2000. A Double-Difference Earthquake Location
709 Algorithm : Method and Application to the Northern Hayward Fault , California.
710 Bull. Seismol. Soc. Am. 1353–1368.
711 Wei, D., Seno, T., 1998. Determination of the Amurian plate motion. Mantle Dyn. plate
712 Interact. East Asia 27, 337–346.
713 Wessel, P., Smith, W.H.F., 1998. New, improved version of generic mapping tools

714 released. Eos, Trans. Am. Geophys. Union 79, 579–579.
715 https://doi.org/10.1029/98EO00426
716 Wesson, R.L., 1987. Modelling aftershock migration and afterslip of the San Juan
717 Bautista, California, earthquake of October 3, 1972. Tectonophysics 144, 215–229.
718 https://doi.org/10.1016/0040-1951(87)90019-9
719 Wetzler, N., Lay, T., Brodsky, E.E., Kanamori, H., 2018. Systematic deficiency of
720 aftershocks in areas of high coseismic slip for large subduction zone earthquakes.
721 Sci. Adv. 4. https://doi.org/10.1126/sciadv.aao3225
722 Woessner, J., Schorlemmer, D., Wiemer, S., Mai, P.M., 2006. Spatial correlation of
723 aftershock locations and on-fault main shock properties. J. Geophys. Res. Solid
724 Earth 111. https://doi.org/10.1029/2005JB003961
725 Yamashita, T., Knopoff, L., 1987. Models of aftershock occurrence. Geophys. J. R. Astron.
726 Soc. 91, 13–26. https://doi.org/10.1111/j.1365-246X.1987.tb05210.x
727 Yoshida, K., Hasegawa, A., 2018a. Sendai-Okura earthquake swarm induced by the 2011
728 Tohoku-Oki earthquake in the stress shadow of NE Japan: Detailed fault structure
729 and hypocenter migration. Tectonophysics 733, 132–147.
730 https://doi.org/10.1016/j.tecto.2017.12.031
731 Yoshida, K., Hasegawa, A., 2018b. Hypocenter Migration and Seismicity Pattern Change
732 in the Yamagata-Fukushima Border, NE Japan, Caused by Fluid Movement and
733 Pore Pressure Variation. J. Geophys. Res. Solid Earth 123, 5000–5017.
734 https://doi.org/10.1029/2018JB015468
735 Yoshida, K., Hasegawa, A., Okada, T., 2015. Spatially heterogeneous stress field in the
736 source area of the 2011 Mw 6.6 Fukushima-Hamadori earthquake, NE Japan,
737 probably caused by static stress change. Geophys. J. Int. 201, 1062–1071.
738 https://doi.org/10.1093/gji/ggv068
739 Yoshida, K., Hasegawa, A., Okada, T., 2016. Heterogeneous stress field in the source area
740 of the 2003 M6.4 Northern Miyagi Prefecture, NE Japan, earthquake. Geophys. J.
741 Int. 206, 408–419. https://doi.org/10.1093/gji/ggw160
742 Yoshida, K., Hasegawa, A., Okada, T., 2015. Spatial variation of stress orientations in NE
743 Japan revealed by dense seismic observations. Tectonophysics 647, 63–72.
744 https://doi.org/10.1016/j.tecto.2015.02.013
745 Yoshida, K., Hasegawa, A., Okada, T., Iinuma, T., 2014. Changes in the stress field after
746 the 2008 M7.2 Iwate-Miyagi Nairiku earthquake in northeastern Japan. J. Geophys.
747 Res. Solid Earth 119, 9016–9030. https://doi.org/10.1002/2014JB011291
748 Yoshida, K., Hasegawa, A., Yoshida, T., 2016. Temporal variation of frictional strength in
749 an earthquake swarm in NE Japan caused by fluid migration. J. Geophys. Res. Solid

750 Earth 121, 5953–5965. https://doi.org/10.1002/2016JB013022
751 Yoshida, K., Hasegawa, A., Yoshida, T., Matsuzawa, T., 2019a. Heterogeneities in Stress
752 and Strength in Tohoku and Its Relationship with Earthquake Sequences Triggered
753 by the 2011 M9 Tohoku-Oki Earthquake. Pure Appl. Geophys.
754 https://doi.org/10.1007/s00024-018-2073-9
755 Yoshida, K., Saito, T., Emoto, K., Urata, Y., Sato, D., 2019b. Rupture directivity, stress
756 drop, and hypocenter migration of small earthquakes in the Yamagata-Fukushima
757 border swarm triggered by upward pore-pressure migration after the 2011 Tohoku-
758 Oki earthquake. Tectonophysics 769. https://doi.org/10.1016/j.tecto.2019.228184
759 Yoshida, K., Saito, T., Urata, Y., Asano, Y., Hasegawa, A., 2017. Temporal Changes in
760 Stress Drop, Frictional Strength, and Earthquake Size Distribution in the 2011
761 Yamagata-Fukushima, NE Japan, Earthquake Swarm, Caused by Fluid Migration.
762 J. Geophys. Res. Solid Earth 122, 10,379-10,397.
763 https://doi.org/10.1002/2017JB014334
764 Yoshida, K., Taira, T., Matsumoto, Y., Saito, T., Emoto, K., Matsuzawa, T., 2020. Stress
765 Release Process Along an Intraplate Fault Analogous to the Plate Boundary: A Case
766 Study of the 2017 M5.2 Akita-Daisen Earthquake, NE Japan. J. Geophys. Res.
767 Solid Earth 125. https://doi.org/10.1029/2020JB019527
768 Yukutake, Y., Honda, R., Harada, M., Tanada, T., Yoshida, A., 2011. Fluid-induced swarm
769 earthquake sequence revealed by precisely determined hypocenters and focal
770 mechanisms in the 2009 activity at Hakone volcano, Japan. J. Geophys. Res. Earth
771 116, 13. https://doi.org/B04308¥r10.1029/2010jb008036
772 Zhao, D., Huang, Z., Umino, N., Hasegawa, A., Yoshida, T., 2011. Seismic imaging of
773 the Amur-Okhotsk plate boundary zone in the Japan Sea. Phys. Earth Planet. Inter.
774 188, 82–95. https://doi.org/10.1016/j.pepi.2011.06.013